Original Article

Failure analysis of an AISI 316 steel pipe elbow exposed to the weather for three years after 16 years of operating at 515 °C

Flavio Pereira de Moraes [1]
Emanuelle Machado Amaral [1]*
Flávio Beneduce Neto [1]
Angelo Fernando Padilha [1]

Abstract

The failure of an AISI 316 austenitic stainless-steel pipe used in a hydrotreatment plant was investigated. Circumferential cracks starting from outside the pipe and parallel to the weld were identified in the pipe elbow. The failure occurred after three years of plant inactivity and exposure to the atmosphere. The pipe was operated regularly for 16 years at a temperature of 515 °C before failure, having undergone phase transformations that made the steel susceptible to intergranular attack, followed by stress corrosion cracking at room temperature. The preferential precipitation of chromium-rich $M_{23}C_6$ carbides at the grain boundaries allowed the occurrence of sensitization, which, associated with the residual tensile stresses caused by the welding process and the presence of chlorine from industrial atmosphere concentrated under insulation, were responsible for the failure by stress corrosion cracking.

Keywords: AISI 316; Pipe elbow; Stress corrosion; Failure analysis.

Análise de falha de uma curva de tubulação de aço AISI 316 exposta ao tempo por três anos após 16 anos operando a 515 °C

Resumo

Foi investigada a falha de um tubo de aço inoxidável austenítico AISI 316 utilizado em uma estação de hidrotratamento. Trincas circunferenciais partindo do lado externo em uma curva de tubulação e paralelas ao cordão de solda foram detectadas. A falha foi identificada após 3 anos de inatividade da instalação, exposta à atmosfera e temperatura ambiente. O tubo operou por 16 anos regularmente a 515 °C antes da falha, tendo sofrido transformações de fase que tornaram o aço suscetível ao ataque intergranular seguido de trincamento por corrosão sob tensão ao tempo na temperatura ambiente. A precipitação preferencial dos carbonetos ricos em cromo do tipo $M_{23}C_6$ nos contornos de grão foram responsáveis pela sensitização, que associada às tensões residuais de tração causadas pelo processo de soldagem e à presença de cloro proveniente da atmosfera industrial concentrado sob o isolamento térmico foram responsáveis pela falha por corrosão sob tensão.

Palavras-chave: AISI 316; Curva de tubulação; Corrosão sob tensão; Análise de falha.

1 Introduction

Stress corrosion cracking (SCC) is caused by the synergistic action of sustained tensile stress (external, internal, or both) and chemical attack, causing failure in a shorter time than the individual effects would require. SCC is probably the most feared type of local corrosion because it often leads to sudden components failure without any visible changes in the metal surface. Cracks, usually initiated in some surface notches, can propagate along grain boundaries or in a transcrystalline manner in anodic (for example, in media containing halogen ions) or cathodic (such as H_2S, NH_3, and HCN, with the formation of hydrogen) chemical environments [1-3].

Low stacking-fault energy (SFE) face-centered cubic (FCC) metals and alloys are particularly susceptible to SCC. A low SFE obstructs the occurrence of dislocation cross-slip, decreases dislocation mobility, hinders the formation

of dislocation cells, leads to higher levels of internal micro-tension, increases internal energy and Gibbs free energy, and leads to a greater susceptibility of the material to stress corrosion cracking [4,5]. Commercial austenitic stainless steels (ASSs) display SFEs in the range of 15–30 mJ/m², that is, between low and middle SFEs [6,7].

ASSs are subject to various types of corrosion (Table 1), such as general corrosion, pitting corrosion, intergranular corrosion, and stress corrosion cracking; however, SCC is the most frequent cause of failure in 18Cr-8Ni austenitic stainless steels [8]. In ASSs, a strong correlation exists between the degree of sensitization caused by the precipitation of chromium-rich phases, mainly $(Fe,Cr)_{23}C_6$, at the grain boundaries and the susceptibility to stress corrosion cracking [9-11].

The microstructures of ASSs are rarely fully austenitic. After solidification, the microstructures of the most widely used ASSs (AISI types 304, 304L, 316, 316L, 321, and 347) present delta ferrite [12], which is not entirely eliminated during subsequent thermomechanical processing [13]. In turn, the austenite phase can partially transform into two types of martensites (α'-bcc and ε-hcp) induced by cold deformation at room temperature [7,14,15].

In particular, the exposure of AISI 316 steel to temperatures between 500 and 900 °C can cause austenite to partially decompose in carbides —$M_{23}C_6$ and M_6C— and intermetallic phases —such as sigma (σ), chi (χ), and Laves (η)— depending on the temperature and time of the exposure [16-20]. These phase transformations, usually precipitations controlled by atomic diffusion, are often represented by time-temperature transformation (TTT) or time-temperature precipitation (TTP) diagrams. For temperatures between 550 °C and 500 °C and exposure times longer than 100,000 h, the TTP diagram for 316 steel predicts only the presence of $M_{23}C_6$ and possibly of Laves phase [20].

However, if 316 steel contains delta ferrite in its microstructure before aging, the eutectoid decomposition of delta ferrite stringers into sigma and austenite phases occurs much faster than the precipitation of the sigma phase from austenite because the chemical composition of ferrite is

closer to the chemical composition of sigma phase and the atomic diffusion in ferrite is faster than in austenite [21,22].

Although the occurrence of SCC in ASS has been reported, it remains a challenge to detect and control the occurrence of SCC in industrial pipes and equipment. In this study, we analyzed the failure of a 168.3 mm (6-inch nominal pipe size) AISI 316 austenitic steel pipe that operated more than 140,000 h (16 years) at 515 °C in a hydrotreatment plant before remaining for three years out of operation and exposed to the industrial atmosphere at room temperature.

2 Materials and methods

The chemical analysis of the materials investigated in this study was carried out in the laboratories of the company Villares Metals S. A. located in Sumaré (SP), Brazil.

The cracks in the pipe were evidenced using ASTM E165/E165M 2018: Standard Practice for Liquid Penetrant Testing for General Industry [23].

ASTM Practice A262 [24], which consists of oxalic acid etch test for the classification of etch structures of austenitic stainless steels, was used to evaluate the susceptibility to intergranular attack.

Microstructural characterization was performed using three complementary techniques: optical microscopy (OM), scanning electron microscopy (SEM) combined with energy-dispersive spectroscopy (EDS), and X-ray diffraction (XRD).

The metallographic sample preparation consisted of grinding, polishing with diamond suspension of 6, 3, and 1μm and etching. For etching a standard solution (V2A-Beize) was prepared by mixing 100 ml HCl, 10 ml HNO_3 and 100 ml distilled H_2O.

X-ray diffraction analysis of the AISI 316 tube sample was performed using an Empyrean diffractometer (Malvern Panalytical) with copper tube radiation at a voltage of 45 kV, initial and final angles of 10° and 110°, respectively.

3 Results and discussion

Table 2 shows the chemical analysis results (weight-percent, wt.%) of the AISI 316 austenitic steel pipe investigated.

3.1 Failure description

A 168.3 mm external diameter 7.11 mm thick austenitic 316 stainless steel pipe operated flawlessly for more than 140,000 h at 515 °C in a hydrotreatment plant. However, high temperatures facilitated microstructural changes, making the material susceptible to intergranular

Table 1. Different corrosion types experienced in 954 cases in 18Cr-8Ni austenitic stainless steels [8]

Corrosion type	Percentage (%)
Stress Corrosion Cracking	38.0
Pitting Corrosion	25.0
General Corrosion	17.8
Intergranular Corrosion	11.5
Other	7.7

Table 2. Chemical composition (wt.%) of the AISI 316 failed pipe

C	Si	Mn	P	S	Cr	Ni	Mo	Cu	N
0.0325	0.4870	1.5326	0.0224	0.0108	16.5618	11.1366	2.1076	0.3449	0.0288

corrosion. Subsequently, the plant remained out of operation for three years in an industrial atmosphere, which satisfied the conditions required for crack propagation through the pipe wall.

During an inspection, through-thickness cracks initiated on the outer side (Figure 1) were detected approximately parallel to a welding bed in the pipe.

The direction of the cracks was consistent with residual stress introduced by welding and acting parallel to the weld bead.

Other locations in the pipe showed similar cracks.

Residual stresses near weld beads are frequent and can have negative or positive effects [25]. Although the pipe was exposed for a long time at 515 °C, the authors believe that the residual stresses introduced by welding were not completely eliminated by this long exposure (annealing) to high temperature. On the other hand, measurements of residual stresses were not carried out in this work. Additionally, the environment under the thermal insulation blanket (alumina-silicate ceramic fiber) can concentrate corrosive species such as Cl^- because of dry-water cycles originating from environmental exposure.
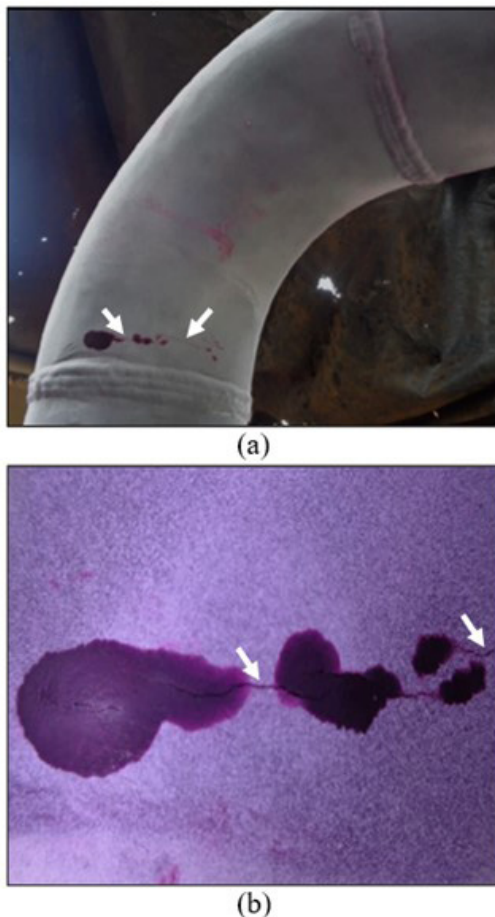

Figure 1. Cracks parallel to circumferential weld revealed during liquid or dye penetrant testing (a) General view showing the cracks' location; (b) Details of the cracks.

3.2 Cracks characterization

Figure 2 shows optical microscopy images of (a) the crack propagation along the grain boundaries and (b) the microstructure after the sensitization evaluation test using ASTM Practice A262.

Etching of the grain boundaries is accentuated as shown in Figure 2b and has been classified, according to the ASTM A262 standard: one or more grains surrounded by ditches. Semi-quantitative chemical microanalysis (EDS) inside the crack (c) shows the presence of sufficient chlorine to cause SCC in ASSs [1,2].

In our opinion, the insulation blanket was responsible for concentrating the chlorine from the industrial atmosphere on the outer surface of the pipe.

3.3 Pipe microstructure characterization

Results of pipe microstructural analysis using OM, SEM/EDS, and XRD techniques are presented below.

3.3.1 Optical microscopy analysis

Observation of the pipe by optical microscopy at low magnification (Figure 3a) reveals the microstructure of the recrystallized grains, which are apparently free of precipitates.

However, when observed at a higher magnification (1000 x), precipitation at the grain boundaries and inside the grains became evident (Figure 3b). According to the literature [16-20], the most favorable sites for the $M_{23}C_6$ precipitation in austenitic stainless steels are grain boundaries, followed by incoherent twin boundaries, coherent twin boundaries and finally at the dislocations within the grains.

3.3.2 Scanning electron microscopy analysis

Observation of the microstructure by SEM using backscattered electrons (Figure 4) revealed the presence of larger colonies of a second phase, or a mixture of two phases, and finer precipitates at the grain boundaries (Figures 4a and 4b), as well as the absence of precipitates on twin boundaries (Figures 4c and 4d).

3.3.3 Energy dispersive spectroscopy analysis

The EDS spectra acquired inside the colony and in the matrix are shown in Figure 5a and 5b. The higher chromium and molybdenum contents and the lower nickel content (compared to the matrix) suggest the presence of the sigma phase inside the colony. EDS was used to identify the fine precipitates at the grain boundaries (Figure 5c, d and e). The higher chromium content in the precipitates compared to the matrix suggests that they were chromium carbides ($M_{23}C_6$).

Table 3 summarizes the chemical compositions at the marked points (areas or spots) analyzed in Figure 5.
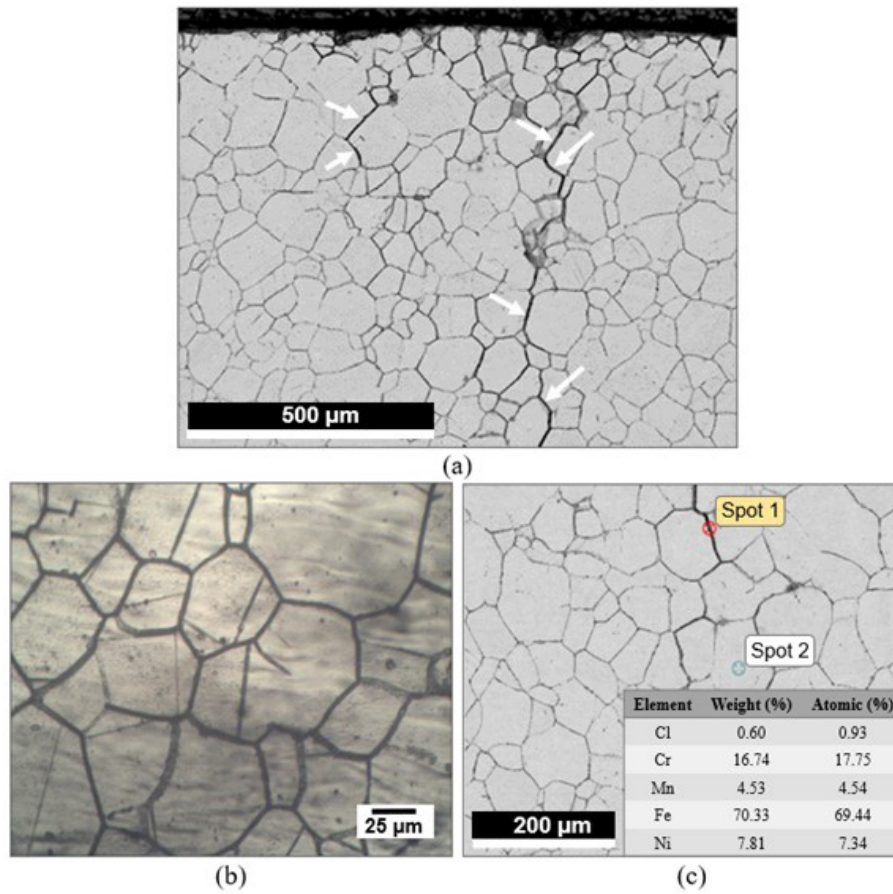
Figure 2. Crack propagation along grain boundaries (a) and ditch-type microstructure was performed after a test following practice ASTM A 262 (b). Analysis performed by SEM/EDS (c) showing the presence of chlorine inside the grain boundary crack (spot 1). Spot 2 showed a typical matrix chemical composition.
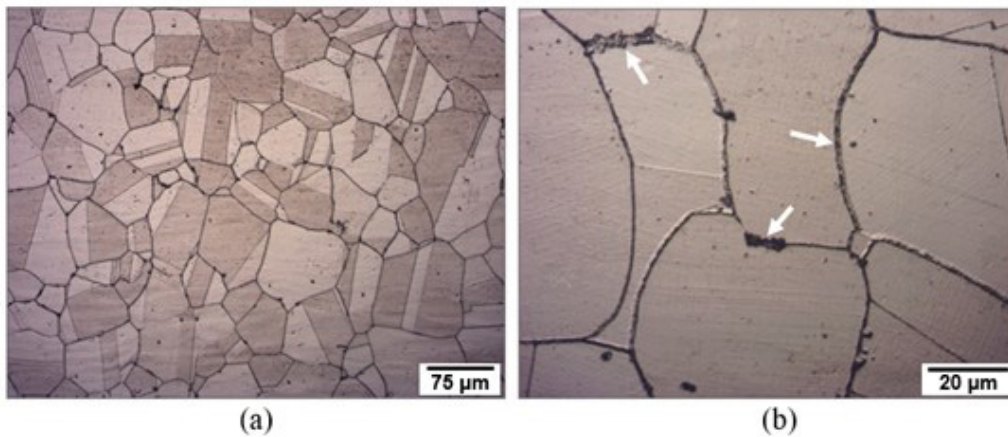

Figure 3. Micrographs obtained by optical microscopy after etching with V2A-Beize at (a) 200 x (b) 1000 x.

Table 3. Chemical composition (wt.%) at the points (areas/spots) analyzed in Figure 5

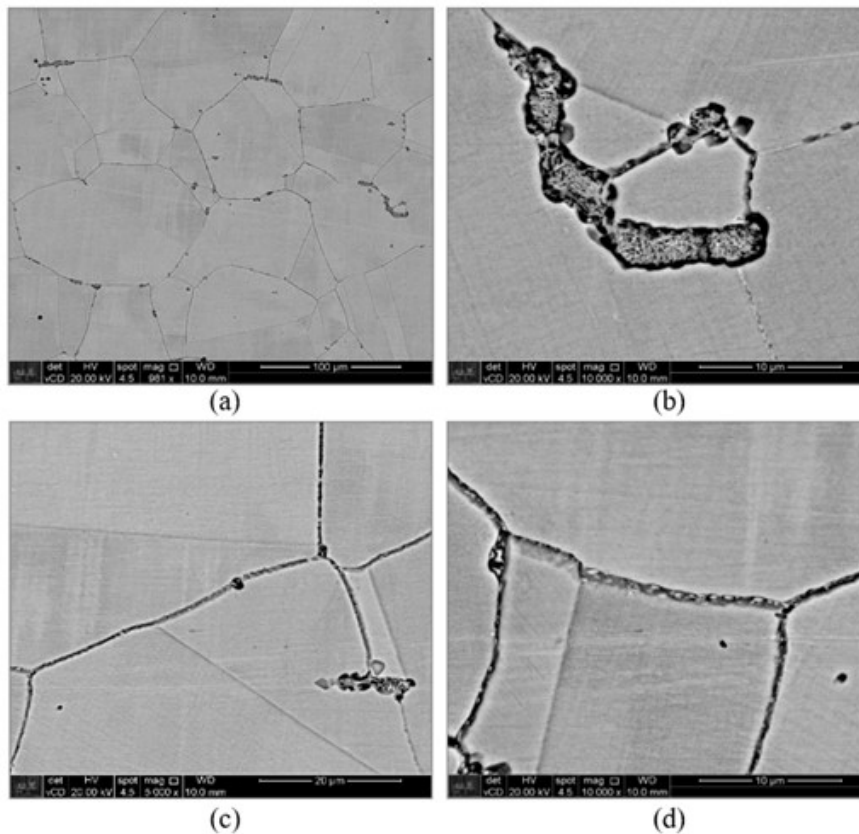| Area/Spot	Fe	Cr	Ni	Mo	Mn	Si
1	31.26	51.43	5.83	8.45	2.03	1.0
2	67.65	18.52	10.26	1.58	1.65	0.36
3	61.77	24.17	9.50	2.80	1.19	0.56
4	50.54	28.12	12.24	5,32	1.71	0.36
5	68.26	18.31	9,68	1.57	1,82	0.36

Figure 4. Micrographs obtained by SEM using backscattered electrons after etching with V2A-Beize. (a) General view of the microstructure; (b) Colonies containing mixed phases; (c) Grain and twin boundaries; (d) Precipitates at the grain boundaries.
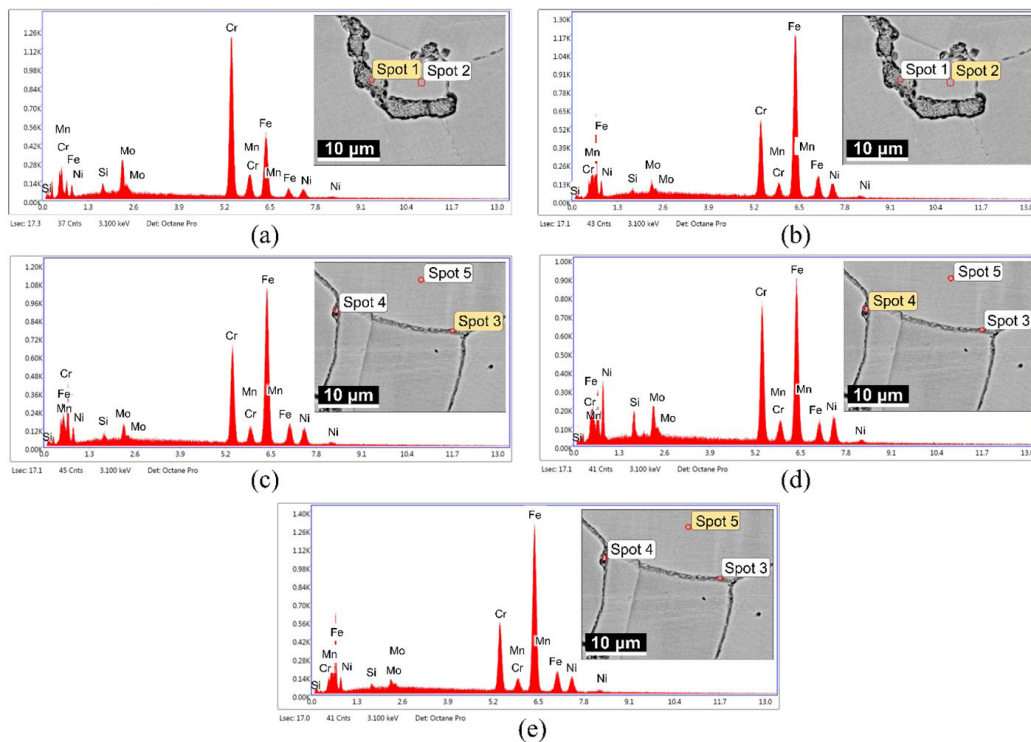

Figure 5. EDS microanalysis in five positions: inside the colony – spot 1 (a); in the matrix – spots 2 and 5 (b and e), and at grain boundaries – spots 3 and 4 (c and d). See the chemical compositions in Table 3.
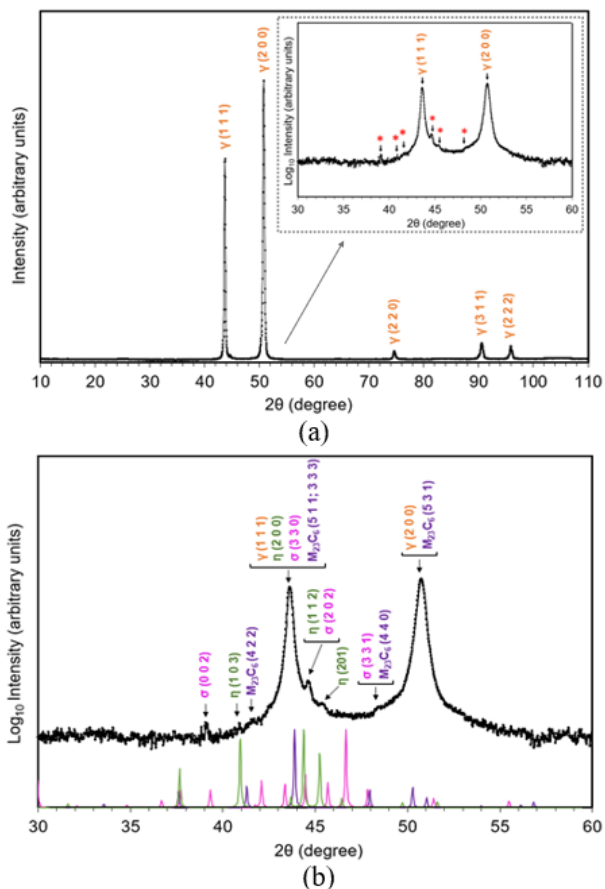
Figure 6. XRD results obtained for the AISI 316 tube sample. Range of (a) 10 to 110 degrees and (b) 30 to 60 degrees superimposed on the positions of the peaks of $M_{23}C_6$ carbide, Laves, and sigma.

The analysis of the EDS spectra shown in Figure 5 and the compositions presented in Table 3, although providing relevant information about the phases present in the microstructure, did not allow for their unequivocal identification, except for the austenitic matrix.

3.3.4 X-ray diffraction analysis

Figure 6 shows a diffractogram of the AISI 316 tube sample. With a logarithmic intensity axis, in addition to (111) and (200) austenite peaks, low-intensity peaks in the 2θ range between 30–60° are observed. Thus, for correct identification, the range between 30–60° in the diffractogram was superimposed on the positions of the peaks of $M_{23}C_6$ carbide (space group Fm-3m or 225),

Laves phase (space group $P6_3/mmc$ or 194), and sigma phase (space group $P4_2/mnm$ or 136) with the aid of previously reported crystallographic data [26-28]

(Figure 6b). Accordingly, Laves phase, $M_{23}C_6$ carbide, and sigma phase were found in the microstructure of the AISI 316 steel sample.

Deighton [29] studied the carbon solubility in AISI 316 steel between 750 and 1100 °C. According to the formula Deighton determined experimentally, carbon solubility was calculated to be approximately 40 ppm at 750 °C and practically zero at 515 °C. Therefore, all the carbon in the steel investigated in this work should precipitate during a long exposition at 515 °C to form $M_{23}C_6$.

Additionally, the experimental TTP diagram for exposure times longer than 100,000 h between 900 and 500 °C [20] does not support the sigma phase presence in the microstructure of AISI 316 steel at 515 °C. However, the presence of delta ferrite before exposure at 515 °C justifies the occurrence of the sigma phase for shorter exposure times [21,22].

4 Conclusions

During exposition at 515 °C, $M_{23}C_6$ (M = Cr, Fe, Ni, Mo) and chromium-rich intermetallic phases precipitated at the austenite grain boundaries, leading to material sensitization. Sensitization alone could not be enough to cause a tube with such robust dimensions to rupture in service. Along with this sensitization, residual welding stresses at the outer surface of the pipe contributed to developing an intergranular stress-corrosion mechanism that resulted in crack formation. Although measurements of residual stresses were not carried out in the present work, it is believed that residual stresses were not fully relieved during the long exposure at 515 °C. The propagation direction of the cracks was consistent with that of the welding residual stresses. Additionally, the environment under the thermal insulation blanket induced the concentration of corrosive agents such as Cl⁻ ions inside the cracks. Therefore, the phase transformations at high temperatures made the steel susceptible to intergranular SCC at room temperature. However, the sigma phase detected in the microstructure is probably not related to a failure by stress-corrosion cracking.

Acknowledgements

References

1 Staehle RW, Avery CH, Beachem CD, Bond AP, Boyd WK, Charley PJ, et al. Stress-corrosion cracking. In: Boyer HE, editor. Metals handbook ASM: failure analysis and prevention. Vol. 10. 8th ed. Ohio: ASM; 1975. p. 205-227.

2 Warke WR. Stress-corrosion cracking. In: Becker WT, Shipley RJ, editors. Metals handbook ASM: failure analysis and prevention. Vol. 11. Ohio: ASM; 2002. http://dx.doi.org/10.31399/asm.hb.v11.a0003553.

3 Pereira HB, Panossian Z, Baptista IP, Azevedo CRF. Investigation of stress corrosion cracking of austenitic, duplex and super duplex stainless steels under drop evaporation test using synthetic seawater. Materials Research. 2019;22(2):e20180211. http://dx.doi.org/10.1590/1980-5373-mr-2018-0211.

4 Thomas KC, Allio RJ. An integrated theory of stress corrosion. Nature. 1965;206(4979):82-83. http://dx.doi.org/10.1038/206082b0.

5 Thompson AW, Bernstein IM. The role of metallurgical variables in hydrogen-assisted environmental fracture. In: Fontana MG, Staehle W, editors. Advances in corrosion science and technology. 1st ed. New York: Springer; 1980. p. 53-175. http://dx.doi.org/10.1007/978-1-4615-9065-1_2.

6 Lu J, Hultman L, Holmström E, Antonsson KH, Grehk M, Li W, et al. Stacking fault energies in austenitic stainless steels. Acta Materialia. 2016;111:39-46. http://dx.doi.org/10.1016/j.actamat.2016.03.042.

7 Tian Y, Gorbatov OI, Borgenstam A, Ruban AV, Hedström P. Deformation microstructure and deformation-induced martensite martensite in austenitic Fe-Cr-Ni alloys depending on stacking fault energy. Metallurgical and Materials Transactions. A, Physical Metallurgy and Materials Science. 2017;48(1):1-7. http://dx.doi.org/10.1007/s11661-016-3839-2.

8 Harada K, Suzuki T, Ishi K. Applications of 18Cr-2Mo ferritic and high chromium ferritic/austenitic stainless steels in Japan. In: Barr RQ, editor. Stainless Steel'77. London: Amax Inc.; 1977. p. 177-184.

9 Gajjar PK, Khatri BC, Siddhpura AM, Siddhpura MA. Sensitization and desensitization (healing) in austenitic stainless steel: a critical review. Transactions of the Indian Institute of Metals. 2022;75(6):1411-1427. http://dx.doi.org/10.1007/s12666-021-02439-8.

10 Nuthalapati S, Kee KE, Pedapati S. Detection and characterization of chloride induced stress corrosion cracking on SS304 under perlite thermal insulation. Materials Research Proceedings. 2023;29:456-471. http://dx.doi.org/10.21741/9781644902516-52.

11 Abou-Elazm A, Abdel-Karim R, Elmahallawi I, Rashad R. Correlation between the degree of sensitization and stress corrosion cracking susceptibility of type 304H stainless steel. Corrosion Science. 2009;51(2):203-208. http://dx.doi.org/10.1016/j.corsci.2008.10.015.

12 Martorano MA, Tavares CF, Padilha AF. Predicting delta ferrite content in stainless steel castings. ISIJ International. 2012;52(6):1054-1065. http://dx.doi.org/10.2355/isijinternational.52.1054.

13 Santos FAM, Martorano MA, Padilha AF. Delta ferrite formation and evolution during slab processing from an 80-ton industrial heat of AISI 304 austenitic stainless steel. REM - International Engineering Journal. 2023;76(1):47-54. http://dx.doi.org/10.1590/0370-44672022760001.

14 Padilha AF, Plaut RL, Rios PR. Annealing of cold-worked austenitic stainless steels. ISIJ International. 2003;43(2):135-143. http://dx.doi.org/10.2355/isijinternational.43.135.

15 Berger A, Egels G, Fussik R, Benito SM, Weber S. A new approach to the optimization of the austenite stability of metastable austenitic stainless steels. Journal of Materials Engineering and Performance. 2023;32(20):9244-9252. http://dx.doi.org/10.1007/s11665-023-08066-2.

16 Weiss B, Stickler R. Phase instabilities during high temperature exposure of 316 austenitic stainless steel. Metallurgical and Materials Transactions. B, Process Metallurgy and Materials Processing Science. 1972;3:851-866.

17 Lai JKL. A study of precipitation in AISI type 316 stainless steel. Materials Science and Engineering. 1983;58(2):195-209. http://dx.doi.org/10.1016/0025-5416(83)90046-0.

18 Minami Y, Kimura H, Ihara Y. Microstructural changes in austenitic stainless steels during long-term aging. Materials Science and Technology. 1986;2(8):795-806. http://dx.doi.org/10.1179/mst.1986.2.8.795.

19 Padilha AF, Rios PR. Decomposition of austenite in austenitic stainless steel. ISIJ International. 2002;42(4):325-327. http://dx.doi.org/10.2355/isijinternational.42.325.

20 National Institute of Materials Science. Creep data sheet. metallographic atlas of long-term crept materials, no. M-2: micrographs and microstructural characteristics of crept specimens of 18Cr-12Ni-Mo stainless steel for boiler and heat exchanger seamless tubes (SUS 316H TB). Japan: NIMS; 2003.

21 Moraes FP, Alves SF Jr, Plaut RL, Padilha AF. Degradation of microstructure and properties of an AISI 316L steel pipe after more than 100,000 hours usage at 640 °C in a petrochemical industry. Procedia Structural Integrity. 2019;17:131-137. http://dx.doi.org/10.1016/j.prostr.2019.08.018.

22 Chen Y, Wei S, Wu D, Lu S. Mechanism of δ-ferrite decomposition in high Si-bearing austenitic stainless steel weld metal during aging at 550 °C. Materials Science and Engineering A. 2023;876:145163. http://dx.doi.org/10.1016/j.msea.2023.145163.

23 American Society for Testing and Materials. ASTM E165/E165M-18: standard practice for liquid penetrant testing for general industry. West Conshohocken: ASTM; 2018. 19 p.

24 American Society for Testing and Materials. ASTM A262-15: standard practices for detecting susceptibility to intergranular attack in austenitic stainless steels. Reapproved. West Conshohocken: ASTM; 2021. 20 p.

25 Barsoum Z, Lundbäck A. Simplified FE welding simulation of fillet welds: 3D effects on the formation residual stresses. Engineering Failure Analysis. 2009;16(7):2281-2289. http://dx.doi.org/10.1016/j.engfailanal.2009.03.018.

26 Berkane R, Gachon JC, Charles J, Hertz J. A thermodynamic study of the chromium-carbon system. Calphad. 1987;11(4):375-382. http://dx.doi.org/10.1016/0364-5916(87)90035-6.

27 Sinha AK, Buckley RA, Hume-Rothery W. Equilibrium diagram of the iron--molybdenum system. Journal of the Iron and Steel Institute. 1967;205:191-195.

28 Yakel HL. Atom distributions in sigma phases. I. Fe and Cr atom distributions in a binary sigma phase equilibrated at 1063, 1013 and 923 K. Acta Crystallographica. Section B, Structural Science. 1983;39(1):20-28. http://dx.doi.org/10.1107/S0108768183001974.

29 Deighton M. Solubility of $M_{23}C_6$ in type 316 stainless steel. Journal of the Iron and Steel Institute. 1970;208:1012-1014.